2023 IEEE 19th International Conference on Body Sensor Networks (BSN) | 979-8-3503-3841-6/23/$31.00 ©2023 IEEE | DOI: 10.1109/BSN58485.2023.10331059

Analytical and computational analysis of a wearable impedance sensor for wireless measurements of analytes in bodily fluids

Mohammad Kafi Kangi
Department of Electrical and Computer Engineering
Michigan State University
East Lansing, MI, USA
kafikangi.m@gmail.com

Xue Jiang
Department of Mechanical Engineering
Rice University
Houston, TX, USA
0000-0002-8908-8963

Elizabeth C. Wilkirson
Department of Mechanical Engineering
Rice University
Houston, TX, USA
0000-0001-5270-6089

Yan Gong
Department of Electrical and Computer Engineering
Michigan State University
East Lansing, MI, USA
gongyan@msu.edu

Peter B. Lillehoj
Department of Mechanical Engineering
Rice University
Houston, TX, USA
lillehoj@rice.edu

Wen Li
Department of Electrical and Computer Engineering
Michigan State University
East Lansing, MI, USA
wenli@msu.edu

***Abstract*—In this paper, we present mathematical and computational analyses of a wearable impedance sensor that can be used for wireless measurement of analytes in bodily fluids. This sensor consists of an interdigitated electrode capacitor as the sensing element and a loop inductor as the antenna. The sensor's resonance frequency was used to evaluate its response during different measurement conditions for mathematical analysis. Computational simulations of the sensor were also performed and the acquired values were compared with the analytical results, which were accurate within 11%. Experimental measurements of *Plasmodium falciparum* histidine-rich protein 2 (*Pf*HRP2), a pathogen-specific protein biomarker, spiked in phosphate buffered saline (PBS) were performed using a wireless impedance sensor prototype, which matched closely with the simulation results. These results demonstrate that the presented mathematical and computational analyses can accurately predict the response of the wireless impedance sensor, making them useful tools for designing wireless impedance sensors for wearable biosensing applications.**

Keywords—Impedance sensor, wearable, wireless, computational simulation, mathematical analysis

I. Introduction

Wearable sensors are a promising technology for the detection and monitoring of a variety of diseases and medical conditions due to their portability and automated operation. In particular, prior works have demonstrated wearable electrochemical sensors capable of rapid and highly sensitive detection of analytes in bodily fluids. Examples include contact lens sensing platforms for glucose monitoring in tears, tattoo-based epidermal sensors for measuring electrolytes in sweat, mouthguards with biosensing elements for salivary uric acid analysis, and microneedle patches for measurements of circulating drugs in the interstitial fluid [1], [2]. However, the need for physical interfacing with a potentiostat/reader limits their portability and comfort in wearable applications. Recently, wearable sensors with wireless sensing capabilities have been demonstrated for the detection of biomolecules, such as glucose, lactate, uric acid, and tyrosine [3], [4]. These devices generally employ an impedance sensor consisting of an interdigitated electrode (IDE) capacitor where the response of the sensor is based on changes in the capacitance/impedance of the IDE.

Prior work has reported analytical equations to model the response of impedance/capacitance sensors [5]; however, the accuracy of these methods is limited since they do not take into account all relevant measurement parameters (e.g., dielectric constants of the sensor substrate and/or sample), which can introduce significant error, especially in absolute measurement applications. To overcome this limitation, we present a complete mathematical analysis of a wearable impedance sensor for wireless measurements which takes into account the dielectric constants of the sensor as well as the sample. The analytical results are compared with those obtained from computational simulations of the sensor, which show good agreement. A wireless impedance sensor prototype was fabricated and used for measurements of *Pf*HRP2, a pathogen-specific protein biomarker, spiked in PBS, which was in excellent agreement (<5% error) with the simulation results. These collective results demonstrate that the proposed mathematical and computational analyses are useful tools for designing wireless impedance sensors for wearable biosensing applications.

II. Experimental Methods

A. Experimental setup

A schematic of the measurement system using the proposed wireless impedance sensor is shown in Fig. 1. The system is comprised of two separate parts: the reader part, which is a coil connected to a vector network analyzer (VNA), and a separate impedance sensor element. The wireless element consists of a metal trace implemented on a printed circuit board (PCB) substrate. The PCB structure contains a coil antenna (inductor) connected to an IDE capacitor. The reader coil is coupled magnetically with the planar coil part of the sensor elements, and the VNA measures the resonance frequency (f_{Res}) of the entire circuit via the reader coil. During the measurement, the IDE region of the sensor is exposed to the liquid sample and its impedance changes due to the different dielectric constants and conductivities of target analytes in the sample. This change will affect f_{Res} of the entire system, therefore by analyzing f_{Res}, we can measure the characteristics of the target analytes.

B. Sensor design and preparation

The IDE and coil antenna consist of 1 μm Au on top of a

This research was funded in part by the Wellcome Trust [215826/Z/19/Z].

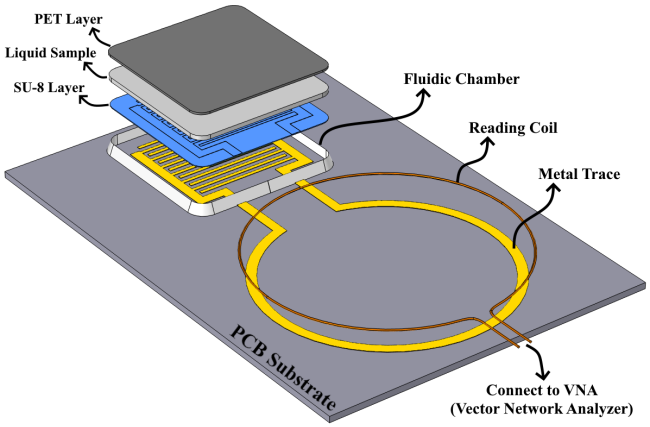

Fig. 1. Exploded view of the measurement system illustrating the components of the wireless impedance sensor.

29 µm-thick Cu layer on a 790 µm-thick epoxy resin-based PCB substrate. A 25 µm-thick layer of SU-8 2025 photoresist was spin-coated, soft-baked, UV cured and post-baked to coat the entire surface of the sensor. SU-8 is used extensively in biosensing applications due to its excellent biocompatibility and mechanical and thermal stability [6]. The SU-8 layer was soaked in isopropanol alcohol for 20 minutes, rinsed in deionized water, dried on a hotplate for 20 minutes at 70°C and plasma treated at 100 W for 15 minutes, which altered its surface roughness and created increased binding areas and binding strengths for antibody-antigen interactions [7]. 5 µL of 100 µg/mL mouse anti- *Pf*HRP2 IgM solution was dispensed on the IDE region and incubated at room temperature for 1 hour, followed by washing with PBS and drying with N_2. 20 µL of StabilBlock™ stabilizer solution was dispensed on the IDE region and incubated at room temperature for 50 minutes, followed by washing with PBS. Sensors were stored in foil pouches with desiccant at 4°C for drying and were ready to use once fully dried.

The IDE region is enclosed by a 7 mm × 7 mm rectangular fluidic chamber to contain the liquid sample. Since the height of the liquid in the fluidic chamber can affect the response of the sensor, a piece of polyethylene terephthalate (PET) film was attached to the top of the chamber to ensure a uniform height of liquid in the chamber during the measurement. In this work, we investigated two measurement conditions. The first was a "dry" condition when there was no liquid sample in the fluidic chamber. The second was a "wet" condition when liquid samples with varying concentrations of *Pf*HRP2 were incubated in the chamber. Cross-sectional images of the sensor during the dry and wet conditions are presented in Fig. 2. In this study, PBS was used as the liquid sample to evaluate the response of the sensor in the wet condition due to its similarity in ion concentration, osmolarity, and pH as human body fluids [8].

C. Experimental measurements

Measurements using the wireless impedance sensor prototype were performed using a NanoVNA system. For the dry condition, the measurement was performed with no liquid sample in the fluidic chamber. For the wet condition, *Pf*HRP2 at 0 ng/mL, 0.1 ng/mL or 1 ng/mL was combined in a 4:1 ratio (*Pf*HRP2 solution:AuNPs) with 40 nm OD-10 gold nanoparticles (AuNPs) labeled with detection antibody (mouse anti-*Pf*HRP2 IgG antibody) following the procedure that we previously reported [12]. To perform the measurement, 20 µL of the *Pf*HRP2-AuNP solution was

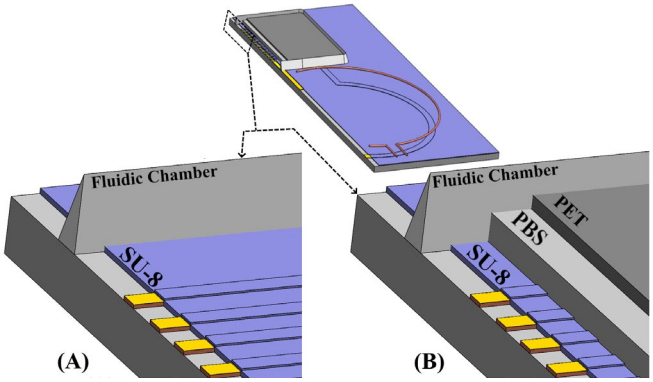

Fig. 2. Cross-sectional images of the impedance sensor in dry (A) and wet (B) conditions.

applied to the IDE region, incubated for 30 minutes, thoroughly washed with PBS and dried with N_2. 30 µL of PBS was added to the fluidic chamber, and PET film was placed on top of the chamber.

III. Mathematical Analysis of the Sensor

The equivalent circuit of the impedance sensor is shown in Fig. 3. In this schematic, L_R refers to the inductance of the reading coil, L_S and R_S are the inductance and resistance of the PCB's antenna coil part, and Z_{IDE} is the impedance of the IDE region. Based on the equivalent circuit model (Fig. 3), the resonance frequency of the impedance sensor can be calculated by (1) [9].

$$f_{Res} = \frac{1}{2\pi}\sqrt{\frac{1}{L_S C_{IDE}} - \frac{(R_S + R_{IDE})^2}{L_S^2}} \tag{1}$$

where R_{IDE} is the real part, and C_{IDE} is the capacitance (imaginary part) of IDE region impedance (Z_{IDE}).

As shown in Fig. 4, the sensor element contains an antenna coil connected to two side paths. Therefore, its inductance (L_S) is estimated as (2)

$$L_S \approx L_{Antenna\ Coil} + 2L_{Side\ Path} \tag{2}$$

The inductance of the antenna coil, $L_{Antenna\ Coil}$, can be predicted by Perry's approximate formula [9]

$$L_{Antenna\ Coil} = \frac{4\pi n^2 a^2}{0.2317a + 0.44b + 0.39c} \tag{3}$$

where n is the number of turns, a is the average radius of the coil, and b and c are the width and thickness of the rectangular cross-section (Fig. 4). On the other side, since the thickness of the metal trace is small, the side paths of the sensor can be considered as two straight tapes and, hence, the inductance of each one can be estimated by (4) [10]

$$L_{Side\ Path} = 2l\left(\log\frac{2l}{b} + \frac{1}{2}\right) \tag{4}$$

where l is the length of the side path, which is illustrated in Fig. 4. In (3) and (4), all of the dimensions are in centimeters,

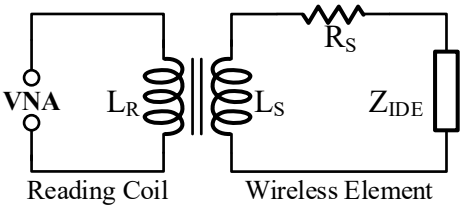

Fig. 3. The equivalent circuit of the wireless impedance sensor.

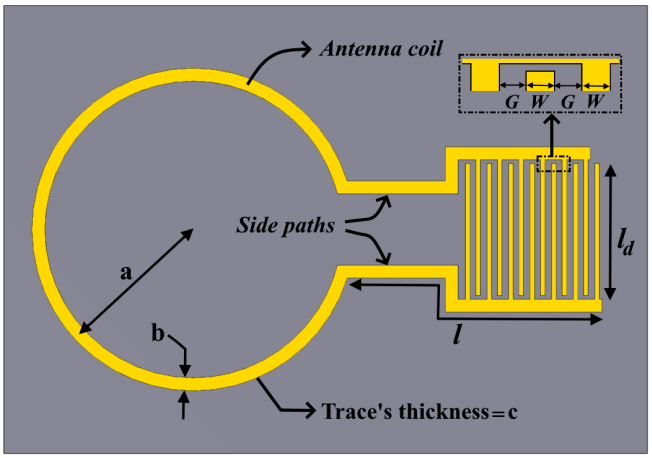

Fig. 4. The defined parameters for computational analysis of the impedance sensor.

and the inductance values are in nanohenry [10]. Based on the basic operation of the sensor (as shown in Fig. 1), the value of L_S remains constant in different test conditions and can be calculated using (2). Similar to $L_{Antenna\ Coil}$, the value of the reading coil's inductance (L_R) can be obtained from Perry's equation; however, to maintain concision, we do not mention it in this paper.

In contrast to L_S and L_R, Z_{IDE} gains different complex values in the dry and wet conditions. In the dry condition, since SU-8 is an insulator with zero conductivity, the R_{IDE} is approximately zero and Z_{IDE} has only a capacitance property (C_{IDE}). C_{IDE} in the dry condition is a multi-layer IDE with N number of electrodes/digits, and its value can be computed using (5) [11].

$$C_{IDE}\big|_{Dry} = (N-3)\frac{C_I}{2} + 2\frac{C_I C_E}{C_I + C_E}\ ,\ N>3 \qquad (5)$$

where C_I is the capacitance of half of one middle electrode with the ground, and C_E is the capacitance between an outer electrode to the ground and, according to [11] and Fig. 5, are estimated based on the effects of the SU-8, air, and PCB layers using (6)

$$C_{I/E} = \underbrace{C_{I/E}\big|_{\substack{h=\infty\\ \epsilon=1}}}_{air\ (Infinite\ layer)} + \underbrace{C_{I/E}\big|_{\substack{h=h_{SU8}\\ \epsilon=\epsilon_{SU8}-1}}}_{SU8\ (Finite\ layer)} + \underbrace{C_{I/E}\big|_{\substack{h=\infty\\ \epsilon=\epsilon_{PCB}}}}_{PCB\ (Infinite\ layer)} \qquad (6)$$

where the h_{SU8} is the thickness of SU-8 layer, and ϵ_{SU8} and ϵ_{PCB} are the dielectric constants of SU-8 and PCB, respectively. The formulas for the finite and infinite layers of C_I and C_E have been presented in [11] and, for simplicity, we do not mention them in this paper. The values of λ, η, and L, which are needed for computing (6), are 2(W+G), W/(W+G), and l_d, respectively. W and l_d are the width and length of the electrode digits, and G is the distance between two near digits (Fig. 4).

In the wet condition, a layer of PBS with different concentrations of the *Pf*HRP2-AuNP conjugates covers the top of the SU-8 layer (Fig. 5B). The presence of the AuNPs forms a conductive layer at the PBS/SU-8 interface while its conductivity changes based on the amount of *Pf*HRP2-AuNP conjugates bound to the IDE region. As such, Z_{IDE} possesses a complex value, including the constant capacitor, C_M, between the IDE region and the PBS layer, interior PBS capacitor and resistor (C_{PBS}, R_{PBS}), and interior parasitic PCB and SU-8 capacitors, which are negligible compared to C_M. Considering d as the distance between the PBS layer and the surface of the electrodes, the C_M can be estimated using (7)

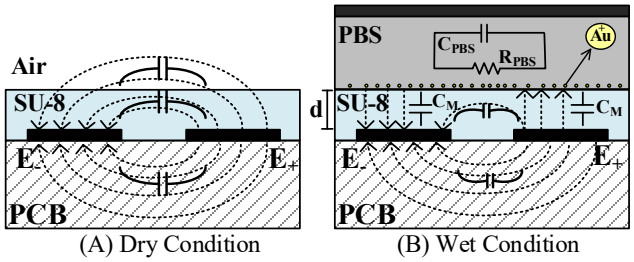

Fig. 5. The main capacitances of the IDE region in the dry and wet conditions.

$$C_M = \epsilon_0 \epsilon_{SU8} \frac{A}{2d} = \epsilon_0 \epsilon_{SU8} \frac{N \times W \times l_d}{2d} \qquad (7)$$

Therefore, the f_{Res} in the wet condition has a constant part which is primarily determined by the C_M capacitor (using (1)) and a variable part based on the values of C_{PBS} and R_{PBS}, which are dependent on the properties of liquid sample and *Pf*HRP2-AuNP conjugates.

IV. Results and Discussion

To perform a comprehensive assessment, we analyzed the sensor using mathematical equations and computational simulations, and compared these with experimental results. Computational simulations were performed using ANSYS HFSS software. A Python program was created for exporting all mathematical equations. A sensor with a design similar to the one shown in Fig. 4 was used for the selected model. The planar electrode structure was modeled as a 1 µm-thick layer of Au on top of a 29 µm-thick layer of Cu on a PCB substrate. The IDE capacitor includes 13 digits (N) with a width (W) of 150 µm, length (l_d) of 4.85 mm, and a distance (G) of 235 µm between the electrodes.

A. Mathematical analysis vs simulation results

The mathematical analysis and simulation of the sensor were performed in dry and wet conditions. For the dry condition, a layer of 40 µm-thick SU-8 was added on the top of the PCB substrate to fill the entire area around the IDE region. An additional 4 µm of SU-8 was added on top of the metal traces to mimic the structure of the real sensor (Fig. 6). For the wet condition, a layer of PBS (210 µm thick) was added on top of the SU-8 layer followed by a 100 µm-thick layer of PET film.

The resonance frequency is the parameter investigated to evaluate the response of the sensor. Hence, we monitored the phase graph of the impedance from the output ports connected to the reading coil to find the f_{Res} of the system for both dry and wet conditions. The simulation results of the sensor are shown in Fig. 7. As shown in this figure, the f_{Res} decreased from 637 MHz in the dry condition to 298 MHz in the wet condition. This reduction in the resonance frequency occurred due to increasing the C_{IDE} in the wet condition and is

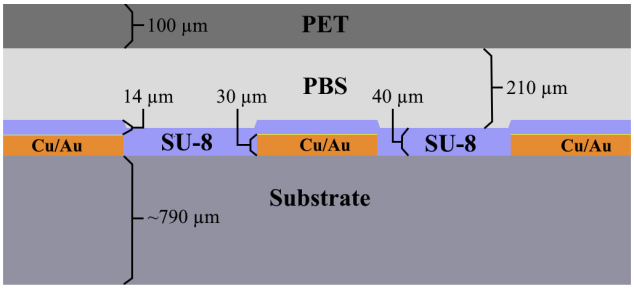

Fig. 6. Thicknesses of the different material layers used in the simulation of the sensor.

consistent with the mathematical analysis of the sensor described in Section III. Additionally, to investigate the effect of the *Pf*HRP2 concentration in the sample, the response of the sensor was simulated using different conductivities, including 1.2 S/m, 1.8 S/m, and 3.4 S/m. The results of these simulations are shown and compared in Fig. 7 and Table. I.

The results obtained from the analytical analysis and the computational simulations are presented in Table I. The analytical values of f_{Res} are similar (accurate within 11% in the dry condition and 3% in the wet condition) with those obtained from the simulation, indicating that the mathematical analysis appropriately predicted the behavior of the impedance sensor. Table I also shows the simulation and analytical results of L_R, L_S, and C_{IDE} to further compare the accuracy of these methods. The simulation values of these components are extracted separately by ANSYS Maxwell.

B. *Experimental results*

Experimental results obtained using the impedance sensor prototype in dry and wet conditions are compared with simulation results in Fig. 7. Distinct phase vs. frequency curves were generated for the dry condition and wet conditions with different *Pf*HRP2 concentrations. Samples with higher *Pf*HRP2 concentrations resulted in a larger shift in the f_{Res} due to the presence of more *Pf*HRP2-AuNP conjugates bound to the IDE region. Additionally, the curves closely resemble those generated by the simulation results (Fig. 7), with a percent difference between the average f_{Res} of 3% and 4.9% in wet and dry conditions, respectively. These results indicate that the presence of more *Pf*HRP2-AuNP conjugates bound to the IDE region effectively increases the conductivity of the PBS/SU-8 interface. The differences between the experimental and simulation results could be due to assumptions made during the analytical and computational calculations, such as component simplifications and material characteristics, as well as experimental factors, such as misalignment of the reading coil and sensor or contamination during sensor fabrication.

V. Conclusions

This study presents mathematical and computational analyses of a wearable impedance sensor that can be used for wireless measurement of analytes in bodily fluids. The sensor's resonance frequency was evaluated through mathematical analyses, computational simulations, and experimental measurements in both dry and wet conditions. An impedance sensor prototype was fabricated and measurements were performed using PBS samples containing varying concentrations of *Pf*HRP2. We demonstrate that the proposed analytical method can accurately predict the simulation and experimental results of the sensor, making it a useful tool for designing wireless impedance sensors for wearable biosensing applications. The results presented in this study can advance the field of wearable and wireless sensors for a variety of clinical applications, including remote patient monitoring and point-of-care diagnoses.

TABLE I. COMPARISION BETWEEN PARAMETERS VALUES ACQUIRED BY SIMULATION AND ANALYTICAL ANALYSIS

Condition		***Parameter***	***Analysis***	***Simulation***	***Experiment***	***Deviation***
-		L_S [nH]	34.5	38	-	9%
-		L_R [nH]	27.6	29.5	-	6.5%
Dry		f_{Res} [MHz]	706	637	600.4	16.5%
		C_{IDE} [pF]	1.46	2.0	-	27%
Wet	0 ng/mL	f_{Res} [MHz]	284	298	290.7	2.3%
		C_{IDE} [pF]	8.97	7.53	-	19%
		σ (S/m)	-	1.2	-	-
	0.1 ng/mL	f_{Res} [MHz]		289	280.7	2.9%
		C_{IDE} [pF]	8.97	7.53	-	19%
		σ (S/m)	-	1.8	-	-
	1 ng/mL	f_{Res} [MHz]		280	270.7	3.4
		C_{IDE} [pF]	8.97	7.53	-	19%
		σ (S/m)	-	3.4	-	-

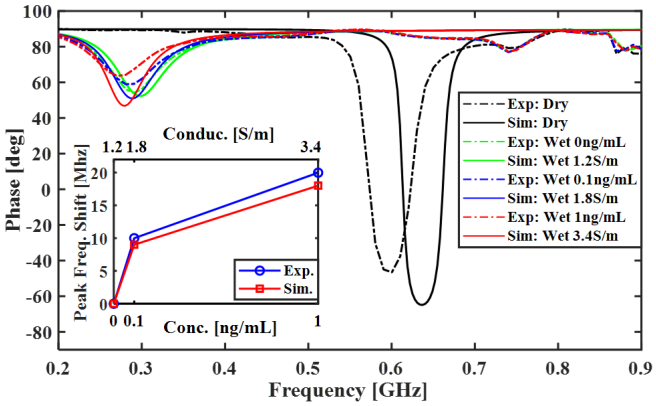

Fig. 7. Comparison between simulation and experimental results of the phase vs. frequency for the wireless impedance sensor in dry and wet conditions. The simulation of the sensor in wet condition was done using different PBS conductivities (1.2 S/m, 1.8 S/m, and 3.4 S/m), and the results are compared with experimental results of wet conditions using PBS spiked with *Pf*HRP2 at 0 ng/mL, 0.1 ng/mL and 1 ng/mL. Inset shows the peak frequency shift of the sensor in wet condition vs. *Pf*HRP2 concentration (experimental) and vs. PBS conductivity (simulation).

References

[1] J. Kim, A. S. Campbell, B. E. F. de Ávila, and J. Wang, "Wearable biosensors for healthcare monitoring," Nat. Biotechnol., vol. 37, no. 4, pp. 389–406, 2019, doi: 10.1038/s41587-019-0045-y.

[2] S. Lin et al., "Wearable microneedle-based electrochemical aptamer biosensing for precision dosing of drugs with narrow therapeutic windows," Sci. Adv., vol. 8, no. 38, pp. 1–14, 2022, doi: 10.1126/sciadv.abq4539.

[3] W. Gao *et al.*, "Fully integrated wearable sensor arrays for multiplexed in situ perspiration analysis," *Nature*, vol. 529, no. 7587, pp. 509–514, 2016, doi: 10.1038/nature16521.

[4] Y. Yang *et al.*, "A laser-engraved wearable sensor for sensitive detection of uric acid and tyrosine in sweat," *Nat. Biotechnol.*, vol. 38, no. 2, pp. 217–224, 2020, doi: 10.1038/s41587-019-0321-x.

[5] A. Qureshi, J. H. Niazi, S. Kallempudi, and Y. Gurbuz, "Label-free capacitive biosensor for sensitive detection of multiple biomarkers using gold interdigitated capacitor arrays," Biosens. Bioelectron., vol. 25, no. 10, pp. 2318–2323, 2010, doi: 10.1016/j.bios.2010.03.018.

[6] Z. Chen and J. B. Lee, "Biocompatibility of su-8 and its biomedical device applications," Micromachines, vol. 12, no. 7, 2021, doi: 10.3390/mi12070794.

[7] I. A. Grimaldi, G. Testa, G. Persichetti, F. Loffredo, F. Villani, and R. Bernini, "Plasma functionalization procedure for antibody immobilization for SU-8 based sensor," Biosens. Bioelectron., vol. 86, pp. 827–833, 2016, doi: 10.1016/j.bios.2016.07.090.

[8] M. D. J. Velásquez-Hernández et al., "Degradation of ZIF-8 in phosphate buffered saline media," CrystEngComm, vol. 21, no. 31, pp. 4538–4544, 2019, doi: 10.1039/c9ce00757a.

[9] M. H. M. Kouhani, J. Wu, A. Tavakoli, A. J. Weber, and W. Li, "Wireless, passive strain sensor in a doughnut-shaped contact lens for continuous non-invasive self-monitoring of intraocular pressure," Lab Chip, vol. 20, no. 2, pp. 332–342, 2020, doi: 10.1039/c9lc00735k.

[10] E. B. Rosa and L. Cohen, "Formulae and Tables for the Calculation of Mutual and Self-Inductance," Bulletin of the Bureau of Standards, Vol. 5, pp 1-132, 1908.

[11] R. Igreja and C. J. Dias, "Analytical evaluation of the interdigital electrodes capacitance for a multi-layered structure," Sensors Actuators, A Phys., vol. 112, no. 2–3, pp. 291–301, 2004, doi: 10.1016/j.sna.2004.01.040.

[12] X. Jiang and P. B. Lillehoj, "Microneedle-based skin patch for blood-free rapid diagnostic testing," Microsystems Nanoeng., vol. 6, no. 1, pp. 1–11, 2020, doi: 10.1038/s41378-020-00206-1.